01 Oct 2022

A Novel Iron Phosphate Cement Derived from Copper Smelting Slag and its Early Age Hydration Mechanism

Yunlong Luo

Xintao Zhou

Zhongqiu Luo

Hongyan Ma
Missouri University of Science and Technology, mahon@mst.edu

et. al. For a complete list of authors, see https://scholarsmine.mst.edu/civarc_enveng_facwork/2271

Recommended Citation

Y. Luo et al., "A Novel Iron Phosphate Cement Derived from Copper Smelting Slag and its Early Age Hydration Mechanism," *Cement and Concrete Composites*, vol. 133, article no. 104653, Elsevier, Oct 2022. The definitive version is available at https://doi.org/10.1016/j.cemconcomp.2022.104653

Cement and Concrete Composites 133 (2022) 104653

Contents lists available at ScienceDirect

Cement and Concrete Composites

journal homepage: www.elsevier.com/locate/cemconcomp

A novel iron phosphate cement derived from copper smelting slag and its early age hydration mechanism

Yunlong Luo [a], Xintao Zhou [a,*], Zhongqiu Luo [a,**], Hongyan Ma [b], Yu Wei [a], Qin Liu [a]

[a] Faculty of Chemical Engineering, Kunming University of Science and Technology, Kunming, Yunnan, 650500, China
[b] Department of Civil, Architectural and Environmental Engineering, Missouri University of Science and Technology, Rolla, MO, 65401, USA

ARTICLE INFO

Keywords:
Copper slag
Iron phosphate cement
Compressive strength
Microstructure
Hydration mechanism

ABSTRACT

Copper slag (CS), a by-product of copper smelting, is normally stockpiled, leading to wastes of resource and space as well as environment pollution. It has not been massively reutilized as a supplementary cementitious material in Portland cement due to its low reactivity. In the present study, CS is for the first time utilized as the base component to prepare an iron phosphate cement (IPC) by reacting with ammonium dihydrogen phosphate (ADP) at room temperature. The influence of the raw materials mass ratio (CS/ADP) on the microstructure and performance of IPC pastes are investigated. It is found that the compressive strength of IPC pastes at all ages is not a monotonic function of CS/ADP, and the paste with CS/ADP of 2.0 gives the highest strengths, i.e., 26.8, 38.9 and 47.5 MPa at 1, 3 and 28 d, respectively. The crystalline phases including $FeH_2P_3O_{10}{\cdot}H_2O$ and $FePO_4$ are formed as the main reaction products to bind the unreacted CS particles. The early age hydration of IPC is found to be a multi-stage process, involving the initial dissolution of ADP and iron-containing phases of CS, the formation of $FeH_2P_3O_{10}{\cdot}H_2O$, the initial generation of $FePO_4$, and the attainment of the hydration reaction equilibrium. Unlike the magnesium phosphate cement, a redox reaction of Fe(II) into Fe(III) occurs due to the suitable range of pH and oxidation-reduction potential of the IPC system during the hydration reaction.

1. Introduction

Phosphate cements, also called chemically bonded phosphate ceramics, were first developed as dental or bone restoration cement materials due to their fast hardening and high early-age strength in the late 19th century. Over the last several decades, many types of phosphate cements have been developed and attracting more and more attention because of their performance merits. For example, because of their fast setting nature and extremely dense microstructure, these materials have been employed for repair and rehabilitation of civil structures [1,2], stabilization of toxic matters (e.g., heavy metals) and nuclear waste and treatment of wastewater [3–5].

Phosphate cements are usually formed by the reactions between an acidic phosphate salt (such as that of potassium, ammonium, or aluminum or phosphoric acid) and a metal oxide (such as that of magnesium, calcium or zinc). Kingery [6] investigated the formation of generalized phosphate cement materials by reacting various inorganic oxides with phosphoric acid solution, and concluded that metal oxides with a weakly basic or amphoteric nature can react with acid phosphates or derivatives of phosphoric acid at room temperature to form a glassy structure. In the recent two decades, Wagh and his coworkers did extensive research works on the reaction mechanisms of three types of phosphate cements through solution chemistry and thermodynamics [7–9]. Among these phosphate cements, magnesium phosphate cement (MPC) was the most widely researched on its performances and properties [10–13], formation mechanism [14–17]. However, its application prospect is severely hindered by its high manufacture cost, which is caused by the high cost of the used chemical agent graded raw materials (MgO and acid phosphate or phosphoric acid) and the high energy-consumption of the necessary dead-burnt pretreatment of magnesia. Therefore, to extend the application of phosphate cement materials, one of the keys is to reduce their cost, say, by finding low-cost, alternative base materials.

It is generally known that iron is one of the most abundant elements, by mass percentage, in the earth crust [18]. Regrettably, iron is rarely used for the manufacture of phosphate cement, and there is totally very limited literature reporting the iron phosphate cement (IPC). In the early 2000s, Wagh investigated the feasibility of using iron oxides for the

* Corresponding author.
** Corresponding author.
E-mail addresses: zhouxt@kust.edu.cn (X. Zhou), luozhongq@kust.edu.cn (Z. Luo).

https://doi.org/10.1016/j.cemconcomp.2022.104653
Received 17 January 2022; Received in revised form 9 May 2022; Accepted 28 June 2022
Available online 4 July 2022

preparation of IPC [9]. It was demonstrated that FeO and Fe_3O_4 can directly react with phosphoric acid or acid phosphate solution at room temperature to form IPC, while Fe_2O_3 cannot be directly used to prepare IPC by reacting with any phosphate solution due to its low solubility even in an acidic solution. Our research group also recently reported the feasibility to prepare IPC by using Fe_3O_4 to react with phosphoric acid solution [19]. In recent years, preparing phosphate cements using silicate minerals-containing industrial solid wastes has become a new hot research topic [20,21], because this not only tackles the environmental pollution caused by the solid wastes but also reduces the manufacturing cost of phosphate cements. In our previous work, iron silicate-contained copper smelting slag was successfully used to prepare a novel acid-base cement, ferrous oxalate cement by reacting with oxalic acid [22,23]. It was found that the iron compounds contained in copper slag (CS), including fayalite and magnetite, can easily react with oxalic acid at room temperature. Inspired by this finding, we propose to prepare iron phosphate cement using CS (as the iron source) and ammonium dihydrogen phosphate (ADP, as the acidic phosphate), which can react at room temperature.

CS is an industrial by-product obtained from the copper smelting and refining process. It is estimated that about 2.0–3.0 tons of CS are generated per ton of copper produced in the smelting process [24]. Every year, around 68.7 million tons of CS is discharged into the environment worldwide, and 20.25 million tons in China [25]. CS contains about 40% iron, most of which exists in the forms of fayalite (Fe_2SiO_4) and magnetite (Fe_3O_4). Unluckily, these forms of iron compounds cannot be easily separated from the slag due to their coexistent state and lower ferromagnetism [26]. Considering the above, CS is often reutilized in the fields of abrasive material, road−base construction, fine and coarse aggregate in concrete by only taking advantage of its physical characteristic (i.e., high hardness) [27]. But these approaches fail to get fully use of its high content of iron and silicon, thus resulting in a huge resource waste. Instead, the reutilization of CS for the preparation of IPC takes fully account of its physical and chemical properties, and, thus, will maximize the values of CS.

This work aims at developing a new type of phosphate cement, iron phosphate cement, by using the iron-rich CS as the only base resource instead of supplementary material. For comprehensively characterizing the new phosphate cement system, this research is divided into two parts: first, experiments are performed on IPC pastes with normal water (W) to cement (C) ratio (W/C = 0.13), and the influences of the raw materials ratio (CS/ADP) on the compressive strength, hydration heat evolution, setting behavior and the formation of hydration product of the cured IPC pastes are holistically investigated; then, the diluted cement suspension with a W/C of 0.7 was adopted to further research the early-age hydration mechanism of IPC by determining the ion (Fe, Si and P) concentrations, pH and oxidation-reduction potentials of the aqueous and solid phase compositions.

2. Materials and methods

2.1. Materials

The starting raw materials used for the preparation of IPC paste and suspension include CS, ammonium dihydrogen phosphate ($NH_4H_2PO_4$, ADP, 99%) and deionized water. CS was supplied by Yunnan Copper Co., Ltd, located in Yunnan, China. CS was firstly dried in an oven at 80 °C for 24 h, and then ground in a ball mill (MTW 110, Shanghai Shibang Machinery Co., Ltd.) for 3 h. The particle size distribution of CS powder was determined using Malvern MASTERSIZER 3000 Analyzer. The mean particle size and BET surface area of the CS powder are 8.50 μm and 1185 m^2/kg, respectively. Its chemical compositions were determined by X-ray fluorescence (XRF, PW 1400 spectrometer, Philips) analysis are given in Table 1. As listed in Table 1, the total amount of iron oxides (Fe_2O_3) and silica (SiO_2) accounts for approximate 81% by weight of CS. In addition, CS also contains little amount of other metal oxides such as magnesium oxide (MgO, 4.99%), aluminum oxide (Al_2O_3, 3.40%) and calcium oxide (CaO, 3.28%). The XRD result shows that the main mineralogical phases of CS are mainly composed of fayalite (Fe_2SiO_4) and magnetite (Fe_3O_4), as well as a certain amount of amorphous phase, as shown in Fig. 1. The ADP used was the purity of 99% and provided by Fengchuan Chemical Reagent Technology Co., Ltd., Tianjin, China.

Table 1
Chemical composition of CS, wt %.

Fe_2O_3	SiO_2	MgO	Al_2O_3	CaO	ZnO	SO_3	Others
58.09	22.84	4.99	3.40	3.28	1.67	1.50	4.23

2.2. Mix design and sample preparation

In this study, IPC pastes and suspension were prepared for the research of the mechanical properties and hydration mechanism. The mix designs are listed in Table 2. For the IPC paste, a CS/ADP mass ratio ranging from 1.0 to 5.0 and the same W/C mass ratio of 0.13 were selected for the sample preparation. According to the mix proportions listed in Table 2, the dry powders with different CS/ADP mass ratio were dry-mixed in a planetary ball mill for 10 min. Subsequently, the deionized water was added to the pre-mixed dry powders at W/C ratio of 0.13 and mixed for another 1 min. Then, the fresh paste mixtures were cast into a stainless-steel mould with a dimension of 20 mm × 20 mm × 20 mm and sealed with plastic sheets. After 3 h, the specimens were demolded and cured under ambient conditions (25 ± 1 °C and RH 60% ± 5). In order to evaluate the water stability of IPC pastes, the specimens were divided into three group and cured under three different curing conditions such as ambient condition (23 ± 2 °C and 55 ± 5% RH), water curing condition (25 ± 0.5 °C, immersed in water) and standard curing condition (25 ± 0.5 °C and 99% RH) till the day of testing. At every testing age, the specimens were taken out to test the compressive strength and characterize the microstructure. However, for the IPC suspension, the even-mixed dry IPC powder with CS/ADP of 2.0 was placed in a sealed beaker and then the deionized water at the W/C of 0.7 was added in and sealed with a lid. The suspension mixture was mechanically agitated until the end of test. It is worth noting that we counted the starting time when the pre-mixed powder was mixed with the deionized water.

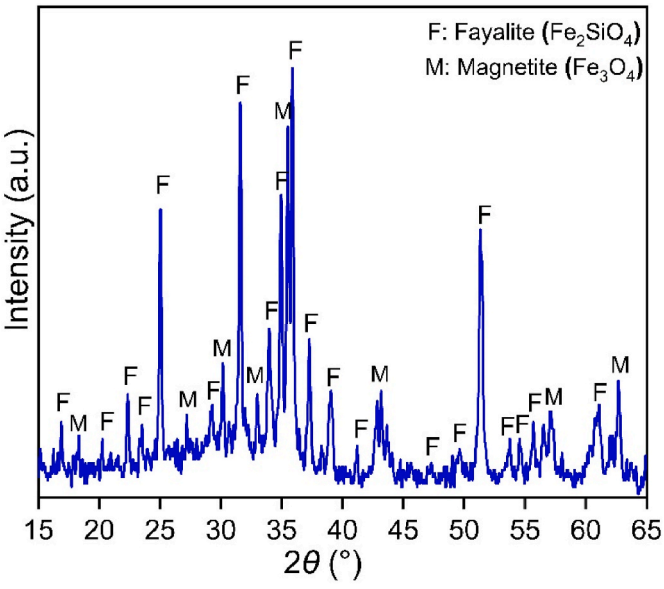

Fig. 1. XRD pattern of CS.

Table 2
Mix proportions and the initial setting time of IPC pastes and suspension.

Sample	CS/ADP (mass ratio)	W/C (mass ratio)	Setting time (min)
IP1.0	1.0	0.13	2.5
IP1.5	1.5	0.13	3.0
IP2.0	2.0	0.13	4.0
IP2.5	2.5	0.13	4.5
IP3.0	3.0	0.13	4.8
IP3.5	3.5	0.13	5.5
IP4.0	4.0	0.13	5.8
IP5.0	5.0	0.13	6.5
IP2.0S	2.0	0.70	–

2.3. Test methods

2.3.1. Setting behavior and compressive strength

The initial setting time of IPC pastes was determined using a Vicat needle apparatus (Jinan Hensgrand Instrument Co., Ltd.) according to GB/T 1346-2011. The hydration heat flows and cumulative hydration heat of IPC paste was monitored by isothermal conduction calorimetry (TAM Air, TA Instruments, USA) at 25 °C. The compressive strengths of the cured IPC paste specimens were tested on a mechanical compression machine (YAW-100D, Jinan Kesheng Machinery Co., Ltd.) with a maximum load of 100 kN at a loading rate of 0.5 kN/S. All the tests were performed on three parallel specimens, and the arithmetic mean value was adopted as the final value for the compressive strength of the specimen.

2.3.2. Suspension analysis

The suspension analysis involves the pH, oxidation–reduction potential (ORP) and ion concentration measurement, and the experimental setup is schematically shown in Fig. 2. The pH change of the suspension with reaction time was recorded by a pH acidity meter (PHS-3C, INESA). ORP was measured by an ORP electrode (ORP-BL, Hangzhou Qiwei Instrument Co., LTD), which is a digital electrode with a refillable Ag/AgCl reference and a built-in temperature sensor. Before determining the pH and ORP, the suspensions were prepared as stated in Section 2.2. The vessel containing the prepared suspension was sealed in order to avoid the possible evaporation of water. The data were recorded at irregular intervals.

For the ion concentration determination, in order to timely obtain the filtrate of the IPC suspension, a disposable syringe filter assembled with a 0.22 μm filter membrane is used to collect and filter the IPC suspension (5 mL) at every set reaction time. Each sampling process usually spends no longer than 10 s. Then the obtained filtrate was immediately acidified with enough nitric acid solution (0.2%, mass concentration) to prevent the precipitation reaction between Fe^{2+} and PO_4^{3-} before determining the ion concentrations. Finally, the ion concentrations were determined by ICP-OES (VISTA-MPX, Agilent, USA).

2.3.3. Characterization of the solid phase

For both IPC paste and suspension systems, the solid phase was firstly characterized by X-ray diffraction (XRD) to evaluate the evolution of mineral phases. The hydration reactions were timely stopped at every set time. For IPC suspension, the suspension samples were separated by centrifugalization, and the remaining solids were soaked in isopropanol for around 1 h to stop the reaction. The final solid phase was obtained after filtration using a Buchner funnel and further drying in an oven at 40 °C and then characterized by XRD. For the paste sample, when cured for 28 d, the sample was crushed and rinsed with isopropanol to stop the reaction, and then filtered under vacuum using a Buchner funnel. The solid phase was dried in an oven at 40 °C and then ground by hand before performing the XRD, thermogravimetry analysis (TG-DTG), Fourier transform infrared spectroscopy (FTIR), and X-ray photoelectron spectroscopy (XPS).

The XRD analysis was carried out using a Bruker D8 Advance device with Cu-Ka radiation (1.5406 Å, 40 kV and 40 mA). The diffraction was performed in the 2 θ range of 10 °–50° with a step size of 0.2°/min. TG-DTG analysis was conducted using a NETZSCH STA 449 F3 device from 30 to 1000 °C at a heating rate of 10 °C/min under a flowing nitrogen atmosphere. FTIR (Tensor 27 Bruker Optics, Germany) was adopted to identify structures on the basis of characterizations of functional groups, and the spectra were obtained by a Bruker Tensor 27 spectrometer in the wavenumber range of 4000–400 cm^{-1} with a resolution of 4 cm^{-1}. The XPS was performed with a Thermo Scientific K-Alphato device to determine the composition and chemical state of CS and 28 d-cured IP2.0 and IP5.0. Survey spectra (pass energy = 150 eV, step size = 1 eV) and high-resolution spectra of C 1s, O 1s, Si 2p, Fe 2p and P 2p (pass energy = 50 eV, step size = 0.1 eV) were collected on a spot size of 400 μm. The morphology of the 28 d-cured IP2.0 and IP5.0 was characterized by scanning electron microscopy/energy-dispersive X-ray spectroscopy (SEM-EDS) and backscattered electron (BSE, Zeiss Sigma 300). For BSE imaging, the paste sample was firstly polished slightly using argon ion polishing (Leica EM TIC 3X) to improve the flatness of the surface, and then dried and vacuum impregnated with low viscosity epoxy resin to solidify the internal microstructure.

3. Results and discussion

3.1. Physical performance and setting behavior of IPC pastes

3.1.1. Compressive strength

The influence of the CS/ADP mass ratio on the strength development of the IPC pastes was investigated, as shown in Fig. 3. The raw materials

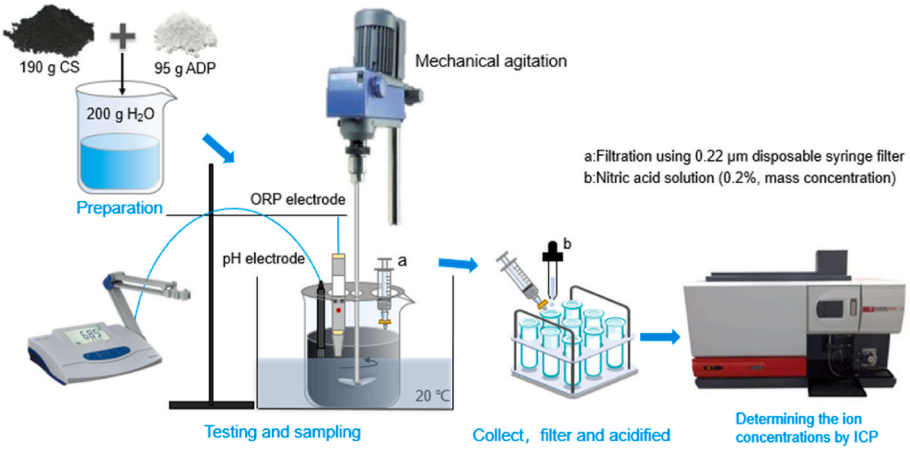

Fig. 2. Experimental setup for the suspension preparation, sampling and determination.

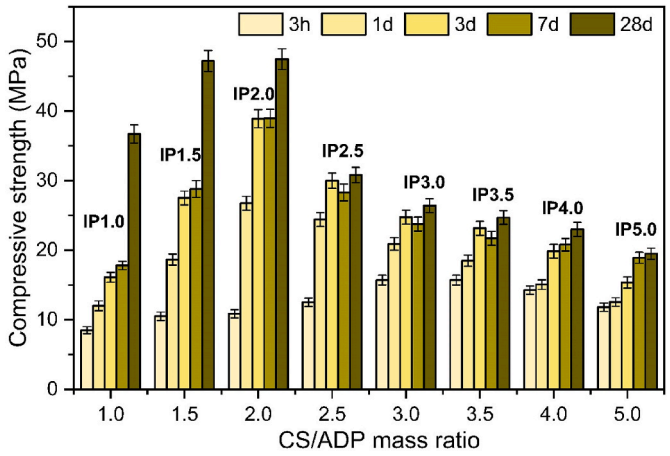

Fig. 3. Influence of CS/ADP mass ratio on the compressive strength of IPC pastes.

ratio had a significant effect on the compressive strength of the IPC pastes. The compressive strength firstly increased, and then decreased with the CS/ADP mass ratio increasing from 1.0 to 5.0. When CS/ADP mass ratio was 2.0, the compressive strengths at all curing ages reached the maximum values, which were 10.9, 26.8, 38.9, 39.0 and 47.5 MPa at 3 h, 1, 3, 7 and 28 d, respectively. The early compressive strength of IPC prepared by CS was higher than that prepared by Fe_3O_4 [19]. Low CS/ADP means that excessive amount of ADP remains unreacted in the IPC paste specimen (IP1.0) and absorbs moisture from the environment, forming high porosity in the microstructure of IPC paste specimen, thus resulting the lower compressive strength. This phenomenon of optimal precursor ratio has been widely found and explained by a three-limit theory [11,28]. It can also be found that the compressive strengths for all specimens keep increasing with the extension of curing age from 7 to 28 d. The compressive strengths for the IPC with lower CS/ADP (1.0–2.0) increase more greatly than those with higher CS/ADP (2.5–5.0). The sufficient amount of ADP in the IPC pastes can still react with the iron compounds contained in CS to form more hydration products at later age in the IPC pastes with lower CS/ADP mass ratio.

Water stability is always a matter of concern for the wide application of phosphate cement materials [29]. Therefore, we evaluated its water stability performance by using strength retention coefficient, which is defined by the ratio of 28 days compressive strength of the specimen cured under water condition or standard curing condition to that cured under the ambient condition. The result is shown in Fig. 4. It can be seen that the cured condition has great influences on the compressive strength of IPC pastes. Comparing to that of IPC pastes cured at ambient condition, the 28 days compressive strength presented a decline of different degree under standard curing condition and water curing condition. The strength retention coefficient is also dependent on the CS/ADP ratio. When the CS/ADP is at higher level (no less than 3.0), the prepared IPC paste has better water stability, and the strength retention coefficient is up to 0.918 under water curing condition. The mechanism of physical property degradation will be detailly discussed in our next submitted manuscript.

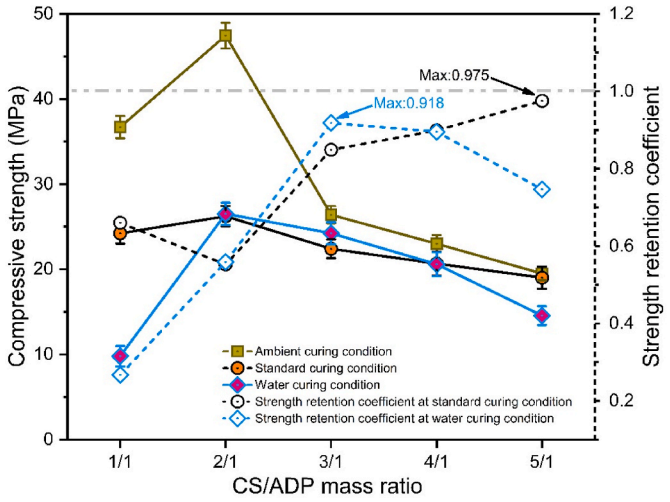

Fig. 4. The compressive strength (28 days) and strength retention coefficient of IPC pasts with different CS/ADP cured under different conditions.

3.1.2. *Hydration heat evolution and setting behavior of IPC*

The isothermal heat rate and cumulative heat of the IPC paste with different CS/ADP ratios are shown in Fig. 5. Due to the rapid hydration process of IPC paste, we only measured the isothermal heat rate within 55 h was measured. As seen from Fig. 5a, an endothermic heat event is observed during the first few minutes for all IPC pastes due to the dissolution of ADP in water and the ionization of $H_2PO_4^-$ (Eq. (1)–(2)).

$$NH_4H_2PO_4 \rightarrow NH_4^+ + H_2PO_4^- \qquad \Delta H = 3.88\ \text{kJ mol}^{-1} \tag{1}$$

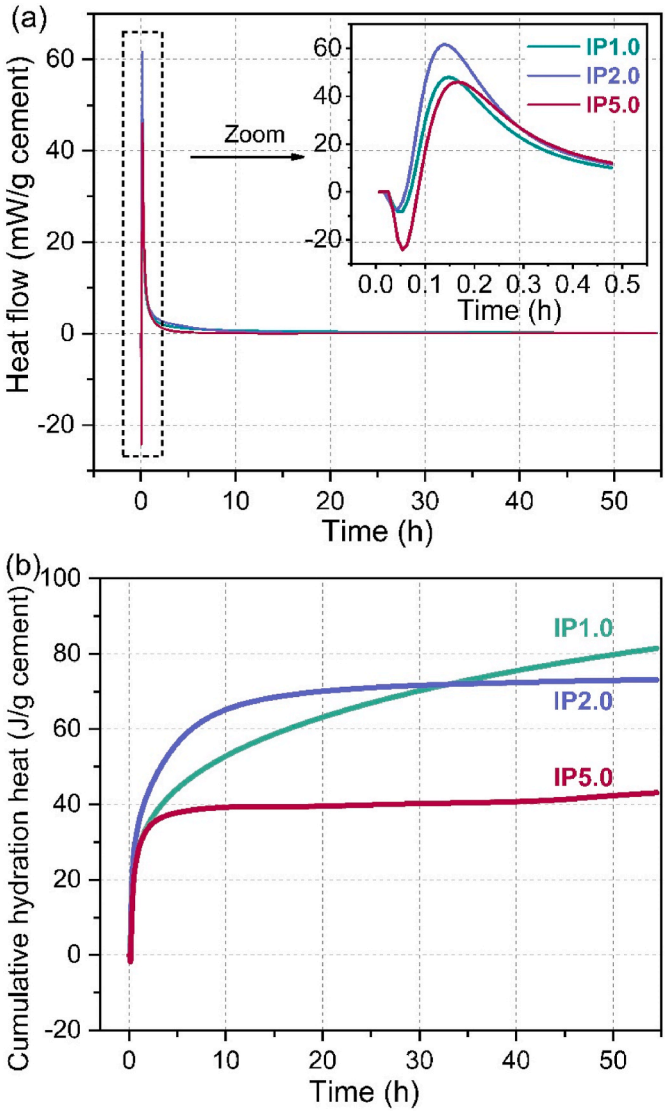

Fig. 5. Effect of the CS/ADP ratio on the hydration heat evolution of IPC pastes. (a) hydration heat evolution rate; (b) cumulative hydration heat.

$$H_2PO_4^- \rightarrow H^+ + HPO_4^{2-}\ \Delta H = 0.99\ kJ\ mol^{-1} \quad (2)$$

It is interesting to find that the endothermic effect of IP5.0 is higher than that of IP1.0 and IP2.0, which apparently inconsistent with the expectation that the lower CS/ADP, the higher endothermic heat amount. The above result can be addressed from the following aspects: (1) the incomplete dissolution of ADP in IP1.0 due to equal solid to water ratio for all IPC pastes, proved by the XRD results of the cured IPC pastes; (2) the slower hydration for IPC paste with higher CS/ADP mass ratio according to Table 2 (initial setting time: IP5.0, 6.5 min; IP2.0, 4 min; IP1.0, 2.5 min), there may be some overlap between the endothermic process and subsequent exothermic process for IP1.0 and IP2.0.

The dissolution of ADP and its ionization in water can provide acidic environment for the IPC paste [30], which facilitates the dissolution of iron oxide and metal silicates contained in CS in water (Eq. (3)–(4)). Their reaction enthalpy data indicate that these dissolution reactions are exothermic. Hence, a distinct exothermic peak can be detected on the heat evolution curves. Moreover, the dissolution of ADP and metal silicates generates large amount of phosphate (HPO_4^{2-}, HPO_4^-, PO_4^{3-}) and metal ions (Fe^{2+}), both of which can combine to form the precipitations as the binding phase (i.e. $Fe_3(PO_4)_2$, $FeHPO_4$, $Fe(H_2PO_4)_2$) [31]. The precipitation reactions can also make some contribution to the exothermic peak.

$$Fe_3O_4 + 2H^+ \rightarrow Fe^{2+} + Fe_2O_3 + H_2O\ \Delta H = -19.3\ kJ\ mol^{-1} \quad (3)$$

$$Fe_2SiO_4 + 4H^+ \rightarrow 2Fe^{2+} + H_4SiO_4\ \Delta H = -39.9\ kJ\ mol^{-1} \quad (4)$$

As displayed in Fig. 5b, IP5.0 has the lowest cumulative heat due to its low content of ADP. But the almost same cumulative heat is obtained for IP1.0 and IP2.0, despite the higher content of ADP of IP1.0 than IP2.0. As stated above, excess ADP keeps unreacted in IP1.0 within the measured stage (55 h), and cannot contribute to the cumulative heat release. It is worth noting that the heat release for IP1.0 doesn't reach its balance at 55 h. The undissolved ADP can still slowly dissolve and react with CS during the later age. This result is consistent with the strength evolution of IPC pastes shown in Fig. 3.

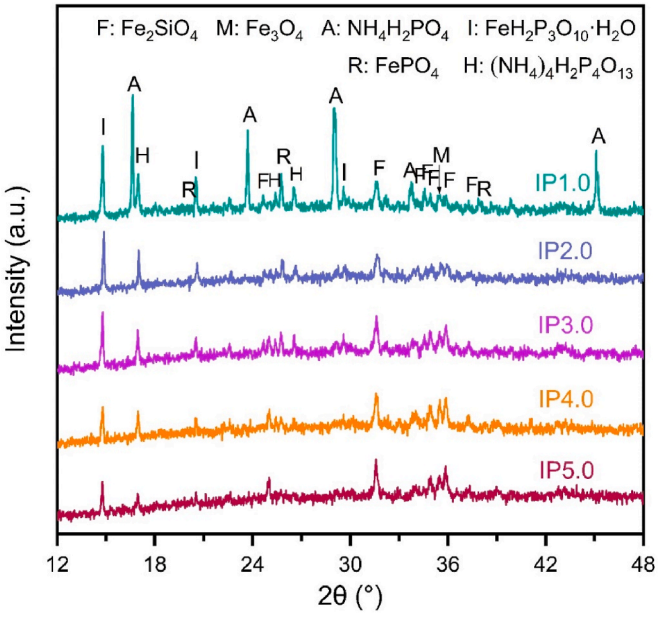

Fig. 6. XRD patterns of the 28 d-cured IPC pastes with different CS/ADP mass ratios.

3.2. Characterization of the 28 d-hydrated IPC pastes

3.2.1. XRD

Fig. 6 shows the XRD patterns of the 28 d-hydrated IPC pastes with different CS/ADP mass ratios. As demonstrated in the figure, iron dihydrogen triphosphate hydrate (IDTH, $FeH_2P_3O_{10}\cdot H_2O$, PDF# 30−0652) can be identified as the main reaction product, which is detected at the 2θ of 14.7°, 20.5° and 29.6°. It was different from the main IPC binder prepared with Fe_3O_4 , which was main amorphous iron phosphate phase [19]. With the decrease of CS/ADP mass ratio, the intensity of its strongest characteristic peak at the 2θ of 14.7° rose sharply, indicating the formation of more hydration product. Beside IDTH, small amount of iron phosphate ($FePO_4$) was formed at low CS/ADP mass ratios, attributed to the reaction between ADP and the magnetite (Fe_3O_4), which usually dissolves at relative highly acidic environment. It is worth mentioning that there is a considerable amount of $(NH_4)_4H_2P_4O_{13}$ formed during the hydration reaction of IPC. Unlike magnesium phosphate cement (MPC) [32], ammonium ion can be incorporated into the crystal lattice of magnesium phosphate salt to form the struvite as the main hydration product for MPC or released as ammonia due to the high pH value of MPC system. For IPC, the released ammonia can be absorbed by the acidic environment of IPC paste and combine with ADP to generate new ammonium phosphate. In addition, the XRD patterns clearly displayed that part of fayalite and magnetite were not involved in the hydration reaction of IPC; this unreacted CS particles could be one source (as the secondary phase) of the mechanical properties of IPC paste [33]. Finally, when CS/ADP mass ratio was 1.0, the presence of residual ADP is very clear. According to Ma et al. [15], the compressive strength of MPC is not determined by a single factor, nor by the amount of hydration products, but by the ratio of MgO, phosphate and water, or by the volume ratio of hydration products in space. Therefore, despite the formation of more hydration product for IP1.0, the existence of unreacted ADP and the loss of the secondary phase (unreacted particles) may lead to the lower strength of the IPC paste, which is consistent with the results of Fig. 3.

3.2.2. TG-DTG

Fig. 7 presents the TG-DTG curves of CS and the 28 d-hydrated IPC pastes with different CS/ADP mass ratios. As shown in Fig. 7, the weight of CS almost keeps unchanged in the measured temperature range of 25–1000 °C, and no water loss and gas emission occur during the heating process. For IPC pastes, an obvious weight loss peak can be observed at about 85.6 °C in the DTG curves, and attributed to the dehydration of the hydration product $FeH_2P_3O_{10}\cdot H_2O$. It can be seen that the maximum weight loss rate increases with the decrease of CS/ADP mass ratio, indicating that the higher reaction degree of CS in the IPC pastes with lower raw material ratio. It can also be observed from TG curves, the weight losses between 85.6 °C and 105 °C are 3.18%, 2.39%, 1.41%, 1.08%, and 0.93% for IP1.0, IP2.0, IP3.0, IP4.0 and IP5.0, respectively. Additionally, a minor peak appears at about 199.6 °C only in the DTG curve of IP1.0, and can be associated with the thermal decomposition of the excess ADP existed in IP1.0 [34]. Then, the slight weight loss occurred at high temperature can be corresponding to the decomposition of $(NH_4)_4H_2P_4O_{13}$.

3.2.3. FTIR

Fig. 8 depicts the collected FTIR spectra of CS powder and IPC pastes with different CS/ADP ratio hydrated for 28 days. For CS, four main vibrations centered at 476, 563, 867 and 962 cm^{-1} were identified, among which the bands around 476 and 563 cm^{-1} represent the ν_4 stretching vibration of Fe–Si–O, and the bands at 867 and 962 cm^{-1} are corresponding to the ν_3 stretching vibration of Fe–Si–O [35,36]. A broad absorption band appeared at 3376 cm^{-1} is attributed to the vibration of O–H bond. After reaction with ADP, the peak intensity of the bands at 476 and 867 cm^{-1} distinctly weaken, and even the band at 962 cm^{-1} disappears, suggesting the part consumption of fayalite during the

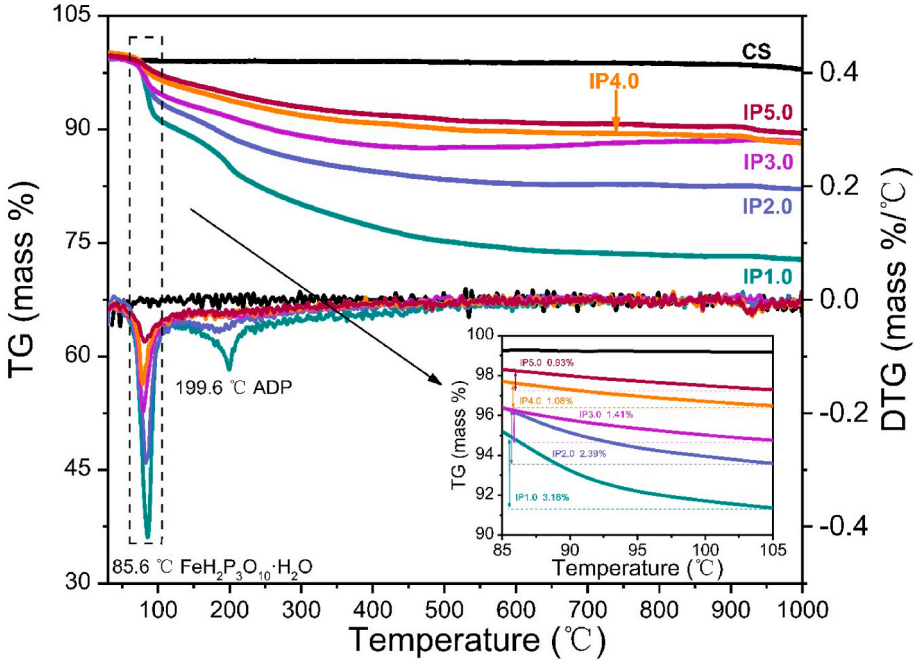

Fig. 7. TG-DTG curves of CS and IPC pastes hydrated for 28 d.

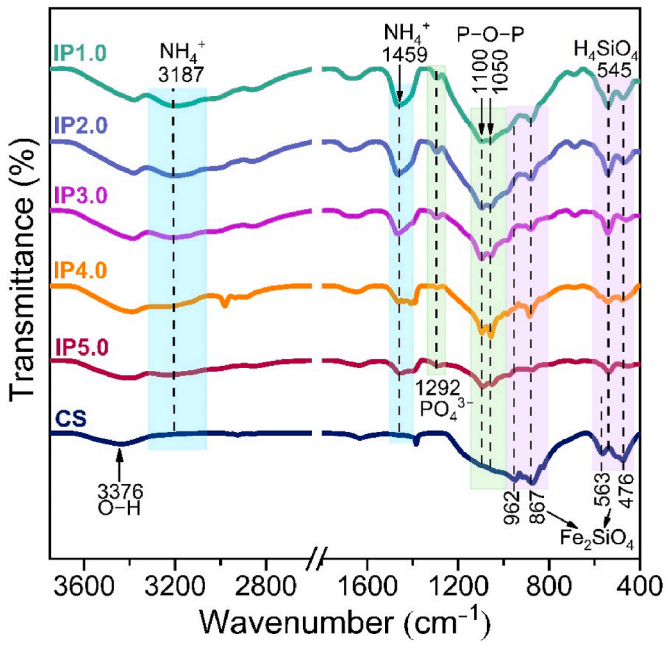

Fig. 8. FTIR spectra of CS and the hydrated IPC pastes at the age of 28 d.

hydration reaction of IPC paste. Meanwhile, the band at 563 cm^{-1} shifts to the lower position of 545 cm^{-1}, and the peak intensity increase with the decrease of CS/ADP ratio, indicating the formation of amorphous H_4SiO_4 through the reaction between fayalite and ADP [37]. The band appeared at 1292 cm^{-1} shows the presence of PO_4^{3-} in the hydrated IPC pastes, while, the peaks at 1100–1050 cm^{-1} are attributed to the stretching vibration of P–O–P [38], and the lower CS/ADP, the higher peak intensity. The bands at 1459 and 3187 cm^{-1} can be assigned to the N–H stretching vibration, confirming the formation of $(NH_4)_4H_2P_4O_{13}$ [39].

3.2.4. XPS

The results of XPS analysis for CS and the 28 d-hydrated IP2.0 and IP5.0 are shown in Fig. 9, and the surface elemental composition of the samples obtained from the spectra is presented in Table 3. As shown in Fig. 9a, O 1s, Fe 2p, and Si 2p signals can be observed at 527–536 eV, 705–735 eV, and 101–106 eV for CS, IP2.0 and IP5.0 samples, respectively. A distinct P 2p signal peak appears at 148 eV for IP2.0 and IP5.0, and its intensity increases with the decrease of CS/ADP ratio. The deconvoluted spectra of Fe 2p, O 1s, Si 2p and P 2p for CS, IP2.0 and IP5.0 are compiled in Fig. 9b, c, d, and e.

According to Fig. 9b, the Fe 2p spectrum of CS illustrates the presence of Fe $2p_{3/2}$ (710.58 eV) and Fe $2p_{1/2}$ (724.8 eV), while for IP5.0 and IP2.0, the peaks corresponded to Fe $2p_{3/2}$ and Fe $2p_{1/2}$ shift toward higher binding energy, and the maximum shifts of binding energy value were 1.42 eV of Fe $2p_{3/2}$ and 0.7 eV of Fe $2p_{1/2}$ for IP2.0. The energy shift between CS and the hydrated IPC paste may be caused by the decrease of the electron density in the relevant atom [40] and the rise of Fe valence state. The spectra could be decomposed into four peaks including one Fe^{3+} peak, one Fe^{2+} peak and two satellite peaks. The percentage of different valence states of Fe was determined by calculating the peak areas and the result was listed in Table 3. The percentage of Fe^{3+} in IPC paste increased by almost 100% in comparison with that in CS, indicating that the happening of the oxidation of Fe^{2+} during the hydration reaction [41]. It can also be found that the percentage of Fe^{3+} rises with the decrease of CS/ADP ratio, suggesting the higher reaction degree of fayalite at the lower CS/ADP ratio, as proved by the XRD result.

Fig. 9c shows the deconvoluted O 1s spectra of CS, IP2.0 and IP5.0. The fitting peaks of CS spectrum appeared at the binding energy of 529.9 and 530.9 eV can be associated with the oxygen atoms forming the Fe–O and Si–O bonds due to the species such as Fe_3O_4 and Fe_2SiO_4 contained in CS. For IP5.0 and IP2.0, the O 1s peak can be deconvoluted into three peaks, among which a peak ascribed to P–O bond appears at around 532.8 eV due to the formation of phosphate phase in IPC paste. As shown from the high-resolution Si 2p spectra (Fig. 9d), the only one peak appeared at 102.3 eV for CS confirms the single Si coordination environment originated from silicates in CS. While the Si 2p spectra of IP5.0 and IP2.0 could be deconvoluted into two components. As proved by FTIR, the newly appeared peak at 103.2 eV can be assigned to the

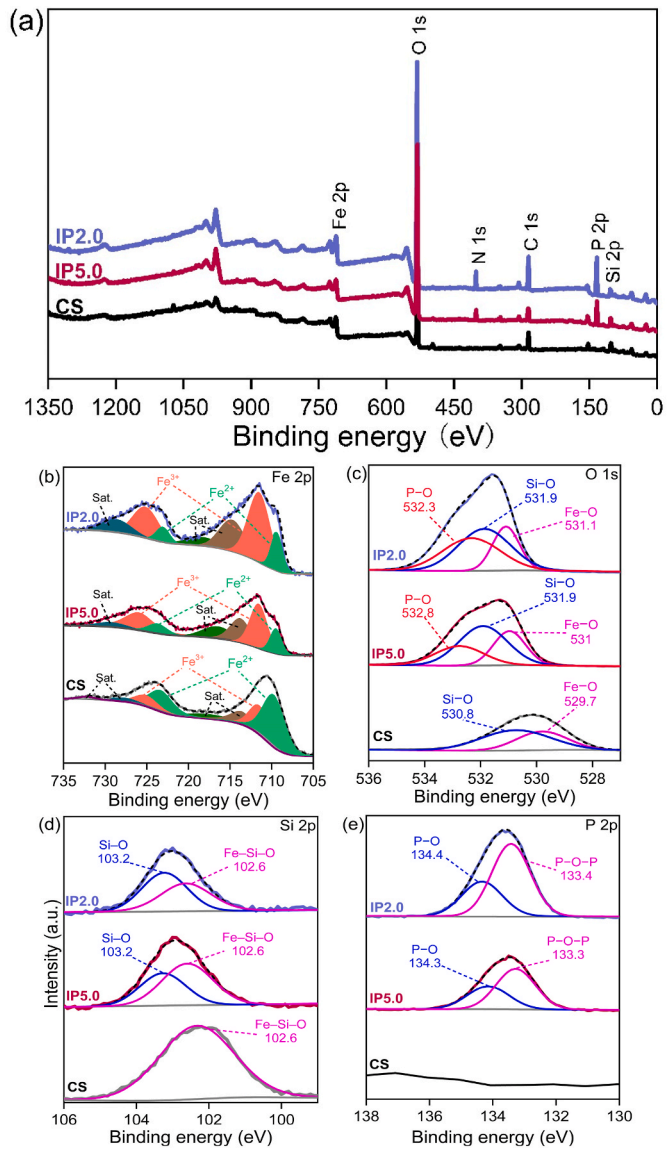

Fig. 9. Full XPS spectra (a), and deconvoluted spectra of Fe 2p (b), O 1s (c), Si 2p (d) and P 2p (e) for CS, IP2.0 and IP5.0.

formation of amorphous H_4SiO_4, as proved by FTIR. As listed in Table 3, the percentage of H_4SiO_4 increases from 41.29% to 54.04% with CS/ADP ratio decrease from 5.0 to 2.0, while the percentage of silicates decreases by 12.75%. The high-resolution P 2p spectra of IP5.0 and IP2.0 are displayed in Fig. 9e, and the peak can be broken down into two components. The first one at lower binding energy (around 133.3 eV) can be ascribed to $FeH_2P_3O_{10}{\cdot}H_2O$. The peak area ratio of $FeH_2P_3O_{10}{\cdot}H_2O$ of IP 5.0 and IP 2.0 accounts for 62.3% and 66.67%, respectively. The second peak at higher binding energy (around 134.3 eV) may arise due to the formation of iron phosphate and little amount of residual ADP in IPC paste. The result echoes the conclusion of XRD.

3.2.5. Microstructure analysis

In order to analyze the microstructure and the phase distribution of the hydrated IPC pastes, SEM-BSE tests were performed on the 28 d-hydrated IP2.0 paste. As shown in Fig. 10a, the polished surface of IP2.0 paste is composed of three parts including irregular-shaped particles, continuous phase and pores. It can be seen that the irregular particles show distinctly dark color on the P mapping, suggesting no P element existed in the particles. But they are rich in Si, O and Fe elements. It is interesting to find that P element is abundant around the particles as a continuous phase, indicating the formation of phosphate as binder phase. Meanwhile, Si element is also contained in the binder phase because the new silicates are formed accompanied by the dissolution of fayalite [37].

EDS tests were also carried out based on the BSE images (Fig. 10b), as listed in Table 4. Many spots were selected to analyze the atomic compositions of different parts. According to the Si/Fe and P/Fe molar ratio, the phase composition can be roughly estimated. The red spots (1–12) sampled from the surface of irregular-shaped particles mainly contain Fe, O, Si, Mg, Ca, etc., but no any amount of P element, suggesting they are unreacted CS particles. The quantitative analysis results show that the Si/Fe ratios are higher than the theoretical Si/Fe ratio of fayalite. It may be caused by the existence of little amount of forsterite (Mg_2SiO_4) and monticellite ($CaMgSiO_4$) in CS. The blue spots (13–14) selected from the continuous phase are composed of Fe, O, Si, P, Mg, Ca, etc. Both of them have similarly low P/Fe ratio, which corresponds to the formation of $FePO_4$. But spot 14 has much higher Si/Fe ratio than spot 13, ascribed to the generation of more amorphous H_4SiO_4 around spot 14. The green spots (15–16) have significantly higher P/Fe ratio than other spots, identifying the abundance of phosphate hydration products ($FePO_4$, $FeH_2P_3O_{10}{\cdot}H_2O$) in this area.

Fig. 10c presents the SEM images of IP2.0 paste hydrated for 28 d. It can be seen that the hydrated IP2.0 paste specimen presents a rather dense structure. Large amount of pentagonal nut-shaped crystals are formed as the binding phase. In combination with the above discussion, the crystal might be $FeH_2P_3O_{10}{\cdot}H_2O$. Moreover, the flocculent gel phase is also formed due to the formation of amorphous H_4SiO_4 as the other binder phase.

3.3. Reaction behavior of CS and ADP at early hydration process

In order to more accurately investigate the reaction mechanism, the evolution of pH, oxidation–reduction potential, ions concentration, and the phase composition of IPC suspension (IP2.0S) were further researched.

3.3.1. pH and the oxidation–reduction potential evolution

The evolution of the pH and ORP of IP2.0S with ongoing hydration is illustrated in Fig. 11. The pH of IP2.0S rapidly decreases from 6.9 to 4.5 during the first 10 s. When the dry premixed raw materials are mixed with water, ADP can easily dissolve and be ionized to release certain amount of protons, resulting a dramatic drop of pH [42]. Then, the pH decreases slowly during the following period of 10 s–100 s, because the dissolution of the fayalite begins and consumes some protons, and thus

Table 3
Elemental composition and chemical state of the elements of Fe, O, Si and P for CS, IP2.0 and IP5.0.

Sample	Elemental compositions (%)					Chemical state of the elements (%)								
						Fe 2p		O 1s			Si 2p		P 2p	
	C	O	Si	Fe	P	Fe^{2+}	Fe^{3+}	P–O	Si–O	Fe–O	Si–O	Fe–Si–O	P–O	P–O–P
CS	28.0	51.5	11.8	8.7	/	64.2	35.8	/	60.0	40.0	/	100.0	/	/
IP5.0	12.2	63.8	6.8	5.2	12.1	37.7	62.3	24.1	48.3	27.7	41.3	58.7	37.7	62.3
IP2.0	14.6	60.8	4.5	5.6	14.5	32.4	67.6	35.9	41.8	22.4	54.0	46.0	33.3	66.7

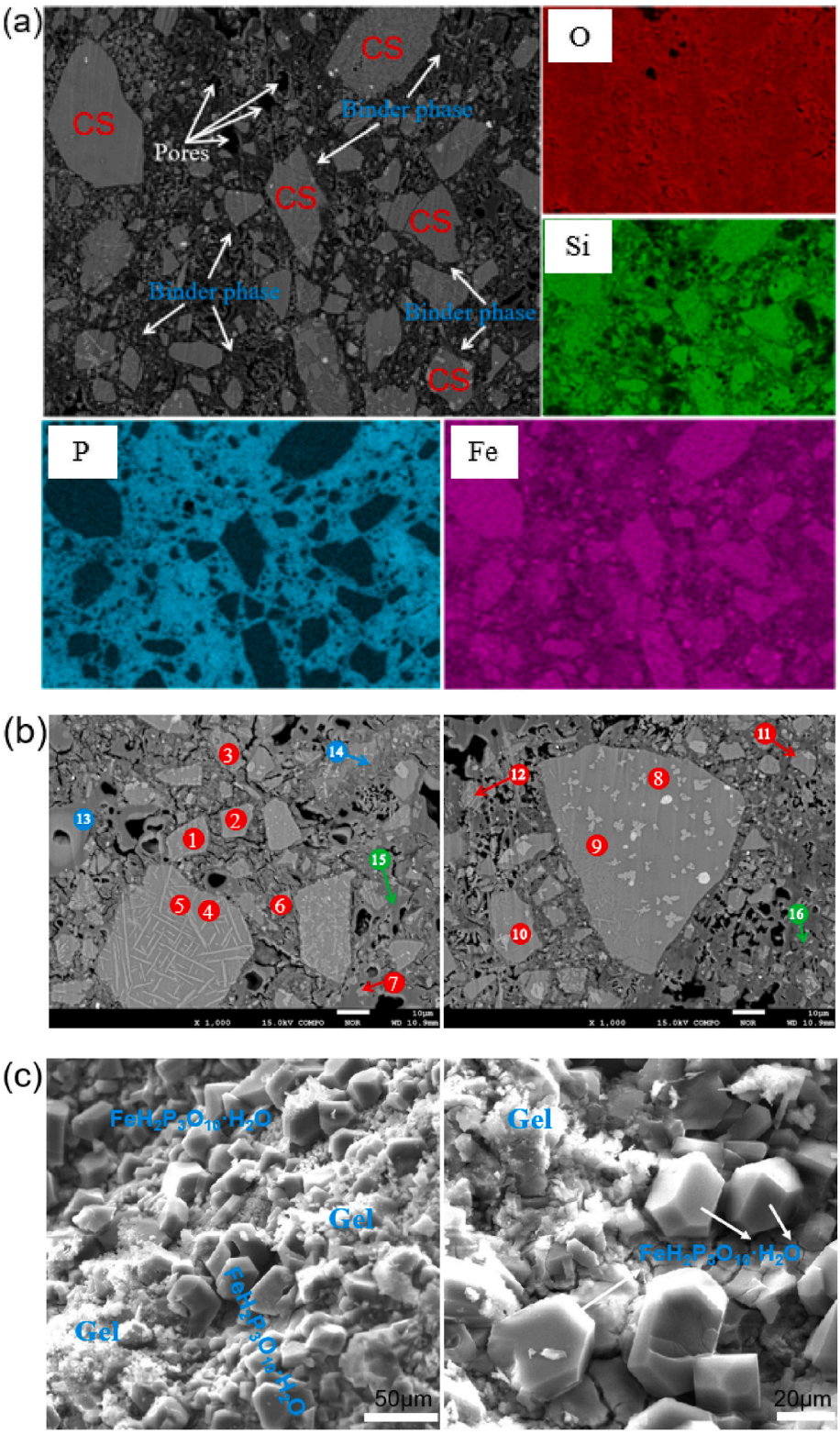

Fig. 10. Element mapping of BSE image (a), element mass percentage analysis of BSE image (b) and (c) SEM images based on the IP2.0 paste cured at 28 d.

slows the rate of pH drop. After that, the dissolution of ADP ends, but the silicate phase continues to dissolve in the acid environment, resulting a slight increase of pH from 4.2 to 4.8 at the stage of 100 s to 3.5 min. Finally, the pH keeps stable after a very slight decrease. It may be caused by the redox reaction happened in the hydration reaction. Herein, we also monitored the evolution of ORP of IP2.0S. The potential continuously decreases until the reaction time of around 2.0 min, then slightly increases and finally reaches a steady platform. For Fe^{3+}/Fe^{2+}, the potential is often inversely proportional to the pH and $[Fe^{2+}]$ of the solution. At the first stage, the evolution of the potential is mainly controlled by $[Fe^{2+}]$; the dissolution of fayalite causes the increase of Fe^{2+}, and thus resulting the decrease of the potential. After 3.5 min, the potential increases slightly, indicating that part of Fe^{2+} is oxidized into Fe^{3+} as the hydration products. The mechanism will be detailly discussed at Section

Table 4
EDS analysis result based on the BSE images (Fig. 10b.).

Spot	Percentage (mass %)								Molar ratio		Possible substances
	Fe	O	Si	P	Mg	Ca	Al	Zn	Si/Fe	P/Fe	
1	43.9	27.1	18.9	0	1.1	2.8	3.4	0	0.58	None	Fe_2SiO_4
2	44.8	27.2	18.9	0	1.1	1.8	3.2	0	−0.95		Mg_2SiO_4
3	50.9	25.5	14.8	0	1.4	2.1	2.7	0			$CaMgSiO_4$
4	42.1	26.6	19.6	0	1.9	2.6	2.9	1.9			
5	47.9	25.8	15.5	0	1.2	2.8	2.7	1.9			
6	41.1	27.9	19.6	0	1.6	4.1	3.3	0			
7	40.6	26.1	14.8	0	1.6	1.9	2.6	0			
8	43.6	27.2	18.8	0	1.7	3.4	3.1	0			
9	44.3	26.6	17.4	0	1.5	3.5	2.8	1.5			
10	42.3	28.5	19.1	0	1.8	3.4	3.1	0			
11	42	27.8	20.0	0	1.6	3.2	3.1	0			
12	42.6	28.5	15.8	0	1.3	2.4	3.0	1.6			
13	37.8	30.6	13.0	11.4	1.0	2.3	2.5	0	0.68	0.55	Fe_2SiO_4; H_4SiO_4
14	25.9	34.3	20.8	7.4	0.7	4.0	4.1	0	1.61	0.52	$FePO_4$
15	23.8	42.2	1.6	30.4	1.1	0	0	0	0.134	2.31	$FePO_4$; H_4SiO_4
16	18.3	39.1	9.9	29.8	0.6	0.8	0.7	0	1.08	2.95	$FeH_2P_3O_{10}{\cdot}H_2O$

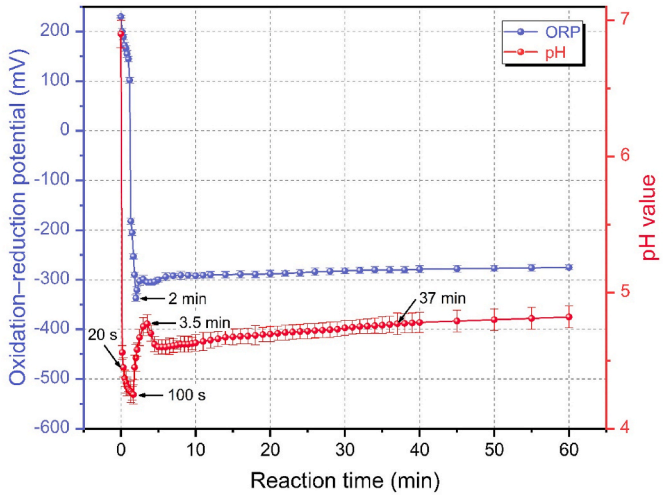

Fig. 11. Evolution of pH and oxidation–reduction potential over time for IP2.0S.

3.4.

3.3.2. Ion concentration evolution

The evolution of the PO_4, Fe and Si concentrations in IP2.0S hydrated within 1 h is shown in Fig. 12a, which is zoomed in the range of 0–240 S (Fig. 12b). The concentration of PO_4 is always higher than that of Fe and Si, and it can reach as high as 3925 mM just at 20 s due to the fast dissolution of ADP. Then all three ions reach their maximum values at around 100 s, but the increasing rate of PO_4 concentration is significantly lower than that of Fe and Si between 20 s and 100 s, indicating that the dissolution of fayalite lags behind that of ADP. This can also explain the slow decrease rate of pH at this stage (20–100 s). After 100 s, the concentrations of Fe and PO_4 start to decrease, confirming the combination of both them to form iron phosphates as the hydration products. The decreasing concentration of Fe and PO_4 concentrations can be divided into two stages including 100 s–3.5 min and 3.5 min–37 min. At the former stage, the concentration of Fe decreases more moderately than that of PO_4, indicating that more PO_4 is incorporated in the formed hydrates, which tentatively verifies the formation of $FeH_2P_3O_{10}{\cdot}H_2O$ in this stage. However, both Fe and PO_4 concentrations show a comparable decrease rate at the latter stage, corresponding to the formation of $FePO_4$. Moreover, the concentration of Si shows a generally growing tendency within the first 10 min, and then remains stable. Between 20 s and 60 s, the concentration of Si always nearly doubles that of Fe due to the dissolution of fayalite (Fe_2SiO_4), revealing that only the dissolution of fayalite occurs, while there is no precipitate reaction happening at this stage. After 80 s, the ratio of Fe/Si in the suspension dramatically decreases below 1, suggesting that part of Fe ion is precipitated by PO_4 ion to form the hydration product. The existence state of Si in the system can be simulated by using Visual Minteq 3.1 software [43]. As shown in Fig. 12c, the dissolved Si mainly exists in the form of H_4SiO_4 in the pH range of 4.2–4.8.

3.4. Discussion of the IPC hydration mechanism

Eh-pH diagrams are the most well-known kinds of stability diagrams to predict reactions that produce the dominant species and may occur under certain conditions. Hence, it is often used to guide the hydrometallurgical technology [44], contaminant removal [45] and metal passivation [46]. Therefore, the Eh-pH diagram (Fig. 13) for the Fe–Si–P–H_2O system at 298.15 K was constructed by using the HSC 6.0 software (a commercial software program, HSC Chemistry, Fairfield, USA) to evaluate the dissolution of the main minerals and the formation of the hydration products in this paper.

As shown in Fig. 13, the upper and lower dashed lines represent the O_2/H_2O and H_2O/H_2 stability boundaries, respectively, meaning that H_2O can only stably exist in the area between these two dashed lines. It should be noted that any species that has some portion of its predominance region within the water stability region is stable with respect to water in the overlapping region [47]. The trends and stability region of solid species such as Fe_2SiO_4 and Fe_3O_4 depicted in Eh-pH diagram are in general agreement with the reported work [44]. It can be seen that the dissolution boundary of Fe_2SiO_4 is a vertical line and appears at pH 6.5, below which it can dissolve to form Fe^{2+} ion. The vertical boundary line also indicates that the dissolution of Fe_2SiO_4 is mainly dependent on the pH instead of the potential of solution. While for the dissolution of Fe_3O_4, the sloped boundary line running from pH = 5.6 (Eh = −143.7 mV) to pH = 6.5 (Eh = −318.1 mV) illustrates that the dissolution of Fe_3O_4 is dependent on both pH and potential of solution and occurs at stronger acidic condition. It means that only a small part of Fe_3O_4 can dissolve in IP2.0S system. Therefore, the dissolution of Fe_2SiO_4 makes the main contribution to provide the iron ions for the formation of hydration products.

In addition, it can be found that the stable domain region of $FePO_4$ becomes larger with the increase of PO_4 concentration, and therefore, the oxidation of Fe^{2+} to Fe^{3+} is much easier at higher PO_4 concentration, and the presence of phosphate enhances the oxidation rate of Fe^{2+}. A kinetic model of the Fe^{2+} oxidation enhanced by phosphate was first

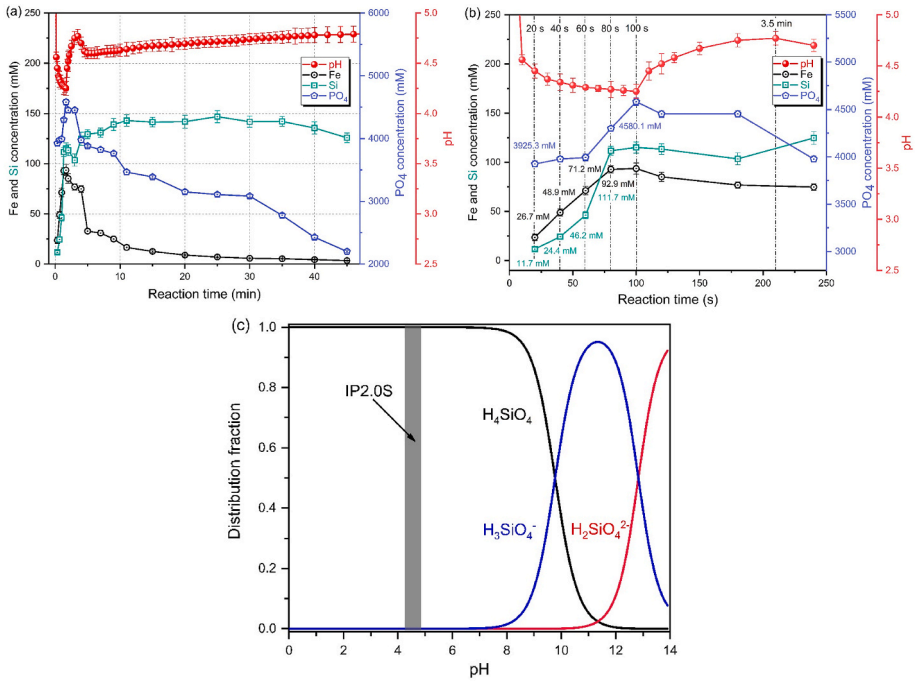

Fig. 12. (a) the evolution of PO_4, Fe and Si concentrations and pH value in IP2.0S system; (b) the zoomed Figure (a) in the range of reaction time of 0–240 s; (c) Ion speciation curves of silicic acid (H_4SiO_4) under different pH condition.

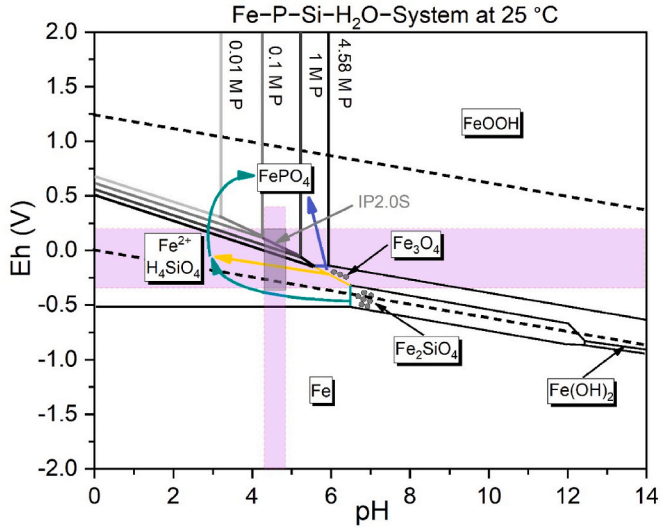

Fig. 13. Eh−pH diagram for the Fe–Si–P–H_2O system at 25 °C and the formation of $FePO_4$ routes (I−III) of IP2.0S.

described as Eq. (5) with the rate constant k=4.5 ± 0.3 atm^{-1} mol^{-2} $L^2 \cdot h^{-1}$ by Cher and Davidson [48]. Due to the exponent on the $[H_2PO_4^-]$ term in Eq. (5), slight increase of $[H_2PO_4^-]$ can bring about a great increase of oxidation rate. Tamura (1976) [49] also proposed a model (Eq. (6)) to describe the relation between the oxidation rate and ions concentrations. Different from Eq. (5), the order of $[H_2PO_4^-]$ varies with its concentration range, when $[H_2PO_4^-] < 0.1$ M, n=1, k=5.02 × 10^9 M^{-3} s^{-1}; when $[H_2PO_4^-] > 0.1$ M, n=2, k=5.02 × 10^{10} M^{-4} s^{-1}. According to these two models, the $[H_2PO_4^-]$ has a positive effect on the Fe^{2+} oxidation rate. The enhancement of Fe^{2+} oxidation by phosphate has been reported widely, especially the influence of phosphate at lower concentration level (0–0.18 mM [50], 70 mg/L [51] or P/Fe (0–2) [52], 0.025–0.5 [53]) on the oxidation rate of Fe^{2+}. For IP2.0S system, the theoretical $[H_2PO_4^-]$ is close to 4.58 mol/L and conducive to form the $FePO_4$ phase as the hydration product according to Eh-pH diagram. The formation of $FePO_4$ can be completed through three routes. In route I, as represented by the green line in the Eh-pH diagram, under the reductive condition with pH below 6.5, Fe_2SiO_4 dissolves and decomposes into Fe^{2+}. After dissolution, $FePO_4$ can be precipitating by promoting the redox potential. In route II (yellow line in Fig. 13), small part of Fe_3O_4 dissolves, releasing part of Fe^{2+}, and then precipitates as $FePO_4$. Moreover, it can be found that there is a short boundary line (Eh = −143.7 mV) between the Fe_3O_4 and $FePO_4$ region, suggesting that Fe_3O_4 can directly transform into $FePO_4$ in the Fe–Si–P–H_2O system at an appropriate condition (route III, blue line in Fig. 12). The transformation can occur in this system when the potential of the solution greater than −143.7 mV. It should be noted that the route III can only happen at higher $[H_2PO_4^-]$ level due to the larger $FePO_4$ predominance region. Instead, there is no boundary line between these two phases at lower $[H_2PO_4^-]$ level, meaning that route III can't be proceeded to form the $FePO_4$ phase. Unfortunately, the species of $FeH_2P_3O_{10} \cdot H_2O$ is not included in the Eh-pH diagram due to the unavailability of its thermodynamic data.

$$-\frac{d[Fe^{2+}]}{dt} = k[Fe^{2+}]Po_2[H_2PO_4^-]^2 \quad (5)$$

$$-\frac{d[Fe^{2+}]}{dt} = k[Fe^{2+}][OH^-][O_2][H_2PO_4^-]^n \quad (6)$$

In order to further investigate the hydration process, the solid phase of the IPC suspension was sampled at different reaction time to conduct the XRD analysis, as shown in Fig. 14. Then, in combination with the results of pH, potential and ions concentration of IP2.0S, the early hydration mechanism of IPC can be deduced as the following four stages:

Stage I (0–100 s): the dissolution of ADP and Fe-containing phases in CS

First, most of ADP quickly dissolves and ionizes in the IPC system at 0–10 s, leading to the sharp decrease of pH value. Then, between 10 s and 100 s, the formed acid environment promotes the start of the dissolution of Fe_2SiO_4 and Fe_3O_4, among which the former takes

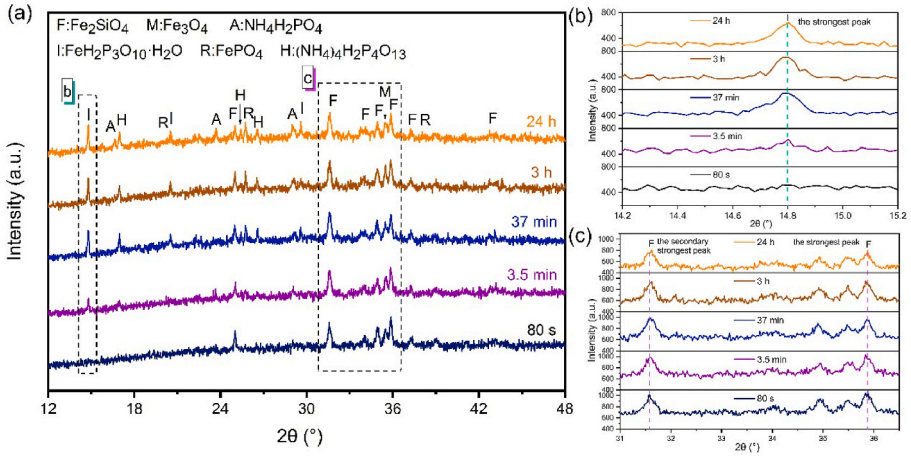

Fig. 14. The XRD patterns of IP 2.0S hydrated for different times, (b) the zoomed XRD patterns at the 2θ range of 14.2°–15.2°, (c) the zoomed XRD patterns at the 2θ range of 31.0°–36.5°.

precedence according to the thermodynamic data ($\Delta_rG°$ (Eq. (4)) = −135.60 kJ/mol, $\Delta_rG°$ (Eq. (3)) = −57.37 kJ/mol, at 298.15 K) and Eh−pH diagram. Meanwhile the rest few ADP continues to dissolve. The simultaneous dissolution of ADP and fayalite and magnetite brings about a slowly decrease of pH value. Their dissolution can be described as Eq. (1)−(4).

Stage II (100 s−3.5 min): the formation of $FeH_2P_3O_{10}·H_2O$ as the hydration product

At this stage, Fe_2SiO_4 continues to dissolve in the acid environment, releasing Fe^{2+} into the solution. Meanwhile, the concentrations of Fe and PO_4 ions start to decrease, suggesting the happening of some precipitation reaction of these two ions. As seen from XRD patterns of the solid phase in IP2.0S (Fig. 14), the characteristic peaks of $FeH_2P_3O_{10}·H_2O$ are observed for the solid phase hydrated for 3.5 min. This result accords closely with the evolution of ions concentrations. The formation reaction can be written as Eq. (7), for which a REDOX reaction between Fe^{2+} ion and O_2 occurred in the presence of PO_4 ion, just illustrating the slight increase of the potential in the reaction time range of 2.0–3.5 min. Moreover, when both Eqs. (3) and (4) reactions are taken together, the increase of pH at this stage is easily accountable.

$$2Fe^{2+} + SiO_4^- + 6H_2PO_4^- + \frac{1}{2}O_2 + 3H_2O \rightarrow 2FeH_2P_3O_{10}·H_2O + H_4SiO_4 + 6OH^- \quad (7)$$

Stage III (3.5–37 min): the new formation of $FePO_4$ as the hydration product

According to Fig. 14b, the intensity of the characteristic peak of continues to increase, indicating the ongoing formation of $FeH_2P_3O_{10}·H_2O$. Meanwhile, $FePO_4$ is newly formed as a hydration product at this stage, as shown in Fig. 14. The formation of the crystal leads to a decrease of pH due to the consumption of OH^- ion for the reaction (see Eq. (8)), while the dissolution of Fe_2SiO_4 and the precipitation of $FeH_2P_3O_{10}·H_2O$ results an increase of pH. Therefore, the pH evolution is determined by all reactions that take place during this stage. According to Fig. 11, the pH shows a trend of first decrease and then increase, indicating that the hydration process during this stage is initially dominated by Eq. (8), and then by Eq. (7). Additionally, according to the Eh-pH diagram, the pH and potential don't reach the conditions for the formation of FeOOH, so there is no FeOOH formed in the IPC suspension system. Thibault et al. [54] also reported that the presence of phosphate could inhibit the formation of FeOOH.

$$2Fe^{2+} + 2H_2PO_4^- + \frac{1}{2}O_2 + 2OH^- \rightarrow 2FePO_4 + 3H_2O \quad (8)$$

Stage Ⅳ (after 37 min): the formation of $(NH_4)_4H_2P_4O_{13}$ and H_4SiO_4

After 37 min, small quantity of $FeH_2P_3O_{10}·H_2O$ is continuously formed according to Eq. (7), leading an increase of pH, also proved by the evolution of pH. The decrease of PO_4 concentration at this stage shown in Fig. 12a is mainly ascribed to the formation of $(NH_4)_4H_2P_4O_{13}$, which can be confirmed by the XRD pattern of the solid at 37 min (Fig. 14). While the decrease of Si concentration may be attributed to the formation of amorphous H_4SiO_4, which also contributes to the improvement of physical property of IPC paste.

4. Conclusion

Iron phosphate cement (IPC) was firstly prepared by using high−iron copper slag (CS) to react with ammonium dihydrogen phosphate (ADP) at room temperature. The influence of CS/ADP on compressive strength and hydration behavior of IPC pastes was investigated. In addition, the structure and the mineral compositions of the hydrated IPC pastes as well as the evolution of ions concentration, pH and oxidation−reduction potential (ORP) of the IPC suspension (w/c = 0.7) were investigated to understand the underlying hydration mechanism. The following conclusions were drawn:

(1) The compressive strength initially increases, and then decreases with the CS/ADP mass ratio increasing from 1.0 to 5.0. When CS/ADP is 2.0, the compressive strength could reach 10.85, 26.75, 38.9, 38.95 and 47.45 MPa at 3 h, 1 d, 3 d, 7 d and 28 d, respectively. The initial setting time was short as 4 min.
(2) The hydration products mainly involve iron dihydrogen triphosphate hydrate ($FeH_2P_3O_{10}·H_2O$), Iron (III) phosphate ($FePO_4$) and little amount of amorphous phase, all which are formed through the reaction between ADP and iron−containing phases such as fayalite and magnetite. XPS analysis indicates that the percentage of Fe (III) in IPC paste increases by almost 100% in comparison with that in CS due to the occurrence of the oxidation of Fe (II) during the hydration reaction.
(3) The XRD analysis results show better consistency between the hydration reaction of IPC suspension and paste. By monitoring the pH, ORP, and ions concentration of the solution and the solid phase of the former paste, it can be concluded that the hydration is a multi−stage process, involving the initial dissolution of ADP

and iron−containing phases in CS (before 100 s), the new formation of $FeH_2P_3O_{10}·H_2O$ (100 s−3.5 min), the starting generation of $FePO_4$ (3.5 min−37 min) and the attainment of the hydration reaction equilibrium.

In this study, CS was firstly used to prepare the iron phosphate cement. The development of this technology is of great significance, not only enriching the kind of phosphate cements, but also greening the preparation of the phosphate cements. The prepared IPC material may have quite potential application prospects as an alternative cementitious material in pavement and construction repair and the solidification/stabilization of hazardous materials due to its fast setting and high early strength. In the future, we will focus on the optimization of the IPC preparation and the durability such as water and heat resistant properties of IPC.

CRediT authorship contribution statement

Yunlong Luo: Conceptualization, Formal analysis, Resources, Validation, Writing – original draft. **Xintao Zhou:** Conceptualization, Methodology, Writing – review & editing. **Zhongqiu Luo:** Writing – review & editing. **Hongyan Ma:** Writing – review & editing. **Yu Wei:** Formal analysis, Software. **Qin Liu:** Software.

Declaration of competing interest

The authors declare that they have no known competing financial interests or personal relationships that could have appeared to influence the work reported in this paper.

Acknowledgements

This research was supported by the National Natural Science Foundation of China (No. 51662024, 21866018), Yunnan Ten Thousand Talents Plan Young & Elite Talents Project (No. YNWR-QNBJ-2018-388 and YNWR-QNBJ-2020-063).

References

[1] S.K. Lee, M.J. Jeon, S.S. Cha, C.G. Park, Mechanical and permeability characteristics of latex-modified fiber-reinforced roller-compacted rapid-hardening-cement concrete for pavement repair, Appl. Sci. Basel. 7 (7) (2017), 694. https://doi.org/10.3390/app7070694.
[2] Q.B. Yang, B.R. Zhu, S.Q. Zhang, X.L. Wu, Properties and applications of magnesia-phosphate cement mortar for rapid repair of concrete, Cement Concr. Res. 30 (11) (2000) 1807–1813.
[3] J.H. Cho, Y. Eom, T.G. Lee, Stabilization/solidification of mercury-contaminated waste ash using calcium sodium phosphate (CNP) and magnesium potassium, J. Hazard Mater. 278 (2014) 474–482.
[4] P. Sanderson, R. Naidu, N. Bolan, J.E. Lim, Y.S. Ok, Chemical stabilisation of lead in shooting range soils with phosphate and magnesium oxide: synchrotron investigation, J. Hazard Mater. 299 (2015) 395–403.
[5] D. Singh, V.R. Mandalika, S.J. Parulekar, A.S. Wagh, Magnesium potassium phosphate ceramic for Tc-99 immobilization, J. Nucl. Mater. 348 (3) (2006) 272–282.
[6] W.D. Kingery, Phosphate Bonding in Refractories, Massachusetts Institute of Technology, 1950.
[7] A.S. Wagh, Chapter 9-Magnesium Phosphate Ceramics, Chemically Bonded Phosphate Ceramics, Elsevier, 2004, pp. 97–110.
[8] A.S. Wagh, Chapter 11- Aluminum Phosphate Ceramics. Chemically Bonded Phosphate Ceramics, Second Edition, Elsevier, 2016, pp. 141–155.
[9] A.S. Wagh, Chapter 12 - iron phosphate ceramics, in: Chemically Bonded Phosphate Ceramics, Second Edition, Elsevier, 2016, pp. 157–164.
[10] H.Y. Ma, B.W. Xu, Z.J. Li, Magnesium potassium phosphate cement paste: degree of reaction, porosity and pore structure, Cement Concr. Res. 65 (2014) 96–104.
[11] H.Y. Ma, B.W. Xu, Potential to design magnesium potassium phosphate cement paste based on an optimal magnesia-to-phosphate ratio, Mater. Des. 118 (2017) 81–88.
[12] A.J. Wang, Z.L. Yuan, J. Zhang, L.T. Liu, J.M. Li, Z. Liu, Effect of raw material ratios on the compressive strength of magnesium potassium phosphate chemically bonded ceramics, Mat Sci Eng. C Mater. 33 (8) (2013) 5058–5063.
[13] B.W. Xu, H.Y. Ma, Z.J. Li, Influence of magnesia-to-phosphate molar ratio on microstructures, mechanical properties and thermal conductivity of magnesium potassium phosphate cement paste with large water-to-solid ratio, Cement Concr. Res. 68 (2015) 1–9.
[14] J.Q. Li, W.X. Zhang, P.J.M. Monteiro, Mechanical properties of struvite-K: a high-pressure X-ray diffraction study, Cement Concr. Res. 136 (2020), 106171. https://doi.org/10.1016/j.cemconres.2020.106171.
[15] H.Y. Ma, B.W. Xu, J. Liu, H.F. Pei, Z.J. Li, Effects of water content, magnesia-to-phosphate molar ratio and age on pore structure, strength and permeability of magnesium potassium phosphate cement paste, Mater. Des. 64 (2014) 497–502.
[16] F. Qiao, Reaction Mechanisms of Magnesium Potassium Phosphate Cement and its Application, PhD thesis, the Hong Kong University of Science and Technology, 2010.
[17] B.W. Xu, B. Lothenbach, A. Leemann, F. Winnefeld, Reaction mechanism of magnesium potassium phosphate cement with high magnesium-to-phosphate ratiod, Cement Concr. Res. 108 (2018) 140–151.
[18] P.A. Frey, G.H. Reed, The ubiquity of iron, ACS Chem. Biol. 7 (9) (2012) 1477–1481.
[19] Y. Wei, X.R. Son, H.W. Jia, Z.Q. Luo, X.T. Zhou, Preparation and characterization of magnetite-based iron phosphate cement, J. Mater. Civ. Eng. 34 (2) (2022), 04021449, https://doi.org/10.1061/(ASCE)MT.1943- 5533.0004046.
[20] Z.Q. Luo, Y. Ma, W.H. Mu, J.H. Liu, J. He, X.T. Zhou, Magnesium phosphate cement prepared with electric furnace ferronickel slag: properties and its hydration mechanism, Construct. Build. Mater. 300 (2021), 123991. https://doi.org/10.1016/j.conbuildmat.2021.123991.
[21] Q.S. Zhang, X. Cao, R. Ma, S.C. Sun, L. Fang, J.H. Lin, J. Luo, Solid waste-based magnesium phosphate cements: preparation, performance and solidification/stabilization mechanism, Construct. Build. Mater. 297 (2021), 123761. https://doi.org/10.1016/j.conbuildmat.2021.123761.
[22] X.T. Zhou, H. He, G.J. Shi, M.Q. Zhang, One kind of copper slag based chemically bonded oxalate phosphate ceramics and its application, China Patent. 7 (2016), 201610310463.
[23] Z.Q. Luo, Y. Ma, H. He, W.H. Mu, X.T. Zhou, W.Y. Liao, H.Y. Ma, Preparation and characterization of ferrous oxalate cement-A novel acid-base cement, J. Am. Ceram. Soc. 104 (2) (2021) 1120–1131.
[24] T.C. Phiri, P. Singh, A.N. Nikoloski, The potential for copper slag waste as a resource for a circular economy: a review-Part II, Miner. Eng. 172 (2021), 107150. https://doi.org/10.1016/j.mineng.2021.107150.
[25] D.Q. Wang, Q. Wang, Z.X. Huang, Reuse of copper slag as a supplementary cementitious material: reactivity and safety, Resour. Conserv. Recycl. 162 (2020), 105037. https://doi.org/10.1016/j.resconrec.2020.105037.
[26] A. Kumar Tiwary, S. Bhatia, A study incorporating the influence of copper slag and fly ash substitutions in concrete, Mater. Today Proc. 48 (2022) 1476–1483. https://doi.org/10.1016/j.matpr.2021.09.293.
[27] R.J. Wang, Q. Shi, Y. Li, Z.L. Cao, Z. Si, A critical review on the use of copper slag (CS) as a substitute constituent in concrete, Construct. Build. Mater. 292 (2021), 123371. https://doi.org/10.1016/j.conbuildmat.2021.123371.
[28] Y. Li, J. Sun, B. Chen, Experimental study of magnesia and M/P ratio influencing properties of magnesium phosphate cement, Construct. Build. Mater. 65 (2014) 177–183.
[29] W.Y. Liao, H.Y. Ma, H.F. Sun, Y. Huang, Y.C. Wang, Potential large-volume beneficial use of low-grade fly ash in magnesia-phosphate cement based materials, Fuel 209 (2017) 490–497.
[30] Y.T. Liu, B. Chen, B.Q. Dong, Y.S. Wang, F. Xing, Influence mechanisms of fly ash in magnesium ammonium phosphate cement, Construct. Build. Mater. 314 Part A (2022), 125581. https://doi.org/10.1016/j.conbuildmat.2021.125581.
[31] A.S. Wagh, S.Y. Jeong, Chemically bonded phosphate ceramics: III, reduction mechanism and its application to iron phosphate ceramics, J. Am. Ceram. Soc. 86 (11) (2003) 1850–1855.
[32] W.W. Han, H.S. Chen, X.Y. Li, T. Zhang, Thermodynamic modeling of magnesium ammonium phosphate cement and stability of its hydration products, Cement Concr. Res. 138 (2020), 106223. https://doi.org/10.1016/j.cemconres.2020.106223.
[33] S.J. Park, H.J. Yim, Evaluation of residual mechanical properties of concrete after exposure to high temperatures using impact resonance method, Construct. Build. Mater. 129 (2016) 89–97.
[34] C.A. Trujillo, N.T. Ramirez-Marquez, J.S. Valencia-Rios, An affordable ammonia temperature-programmed desorption equipment and its calibration using the thermal decomposition of ammonium dihydrogen phosphate, Thermochim. Acta 689 (2020), 178651. https://doi.org/10.1016/j.tca.2020.178651.
[35] Z.H. Yan, Z.P. Sun, J.B. Yang, H.J. Yang, Y.L. Ji, K.Y. Hu, Mechanical performance and reaction mechanism of copper slag activated with sodium silicate or sodium hydroxide, Construct. Build. Mater. 266 Part A (2021), 120900. https://doi.org/10.1016/j.conbuildmat.2020.120900.
[36] S.H. Zhang, N.W. Zhu, F.L. Mao, J.Y. Zhang, X.X. Huang, F. Li, X.Y. Li, P.X. Wu, Z. Dang, A novel strategy for harmlessness and reduction of copper smelting slags by alkali disaggregation of fayalite (Fe_2SiO_4) coupling with acid leaching, J. Hazard Mater. 402 (2021), 123791. https://doi.org/10.1016/j.jhazmat.2020.123791.
[37] Y. Li, X. Zhu, X. Qi, B. Shu, H. Wang, Removal and immobilization of arsenic from copper smelting wastewater using copper slag by in situ encapsulation with silica gel, Chem. Eng. J. 394 (2020), 124833.
[38] M.R. Ahmad, B. Chen, H.J. Duan, Improvement effect of pyrolyzed agro-food biochar on the properties of magnesium phosphate cement, Sci. Total Environ. 718 (2020), 137422. https://doi.org/10.1016/j.scitotenv.2020.137422.
[39] W.Y. Chen, L.L. Wang, G.S. Liu, Synthesis of ammonium polyphosphate with crystalline form V (APP-V) from melamine polyphosphate (MPP), Polym. Degrad. Stabil. 97 (12) (2012) 2567–2570.

[40] A. Mekki, D. Holland, C.F. Mcconville, M. Salim, An XPS study of iron sodium silicate glass surfaces, J. Non-Cryst. Solids 208 (3) (1996) 267–276.
[41] Y.K. Li, X.J. Qi, G.H. Li, H. Wang, Efficient removal of arsenic from copper smelting wastewater via a synergy of steel-making slag and $KMnO_4$, J. Clean. Prod. 287 (2021), 125578. https://doi.org/10.1016/j.jclepro.2020.125578.
[42] H. Lahalle, C. Céline, A. Mesbah, D. Lambertin, C. Cannes, S. Delpech, S. Gauffinet, Investigation of magnesium phosphate cement hydration in diluted suspension and its retardation by boric acid, Cement Concr. Res. 87 (2016) 77–86.
[43] J.C. Westall, J.L. Zachary, F.M.M. Morel, MINEQL. A Computer Program for the Calculation of Chemical Equilibrium Composition of Aqueous System, Mass Inst Tech .Dept Civil Eng Note 18, 1976.
[44] E. Kim, K. Osseo-Asare, Dissolution windows for hydrometallurgical purification of metallurgical-grade silicon to solar-grade silicon: Eh–pH diagrams for Fe silicides, Hydrometallurgy 127–128 (10) (2012) 178–186. https://doi.org/10.1016/j.hydromet.2012.05.013.
[45] A. Bcl, B. Sbk, B. Jkm, Equilibrium calculations for HyBRID decontamination of magnetite: effect of raw amount of $CuSO_4$ on Cu_2O formation, Nucl. Eng. Technol. 52 (11) (2020) 2543–2551.
[46] L.F. Huang, M.J. Hutchison, R.J. Santucci, J.R. Scully, J.M. Rondinelli, Improved electrochemical phase diagrams from theory and experiment: the Ni-water system and its complex compounds, J. Phys. Chem. C 121 (18) (2017) 9782–9789.
[47] L.L. Pesterfield, J.B. Maddox, M.S. Crocker, G.K. Schweitzer, Pourbaix (E–pH-M) diagrams in three dimensions, J. Chem. Educ. 89 (7) (2012) 891–899. https://doi.org/10.1021/ed200423n.
[48] M. Cher, N. Davidson, The kinetics of the oxygenation of ferrous iron in phosphoric acid solution, J. Am. Chem. Soc. 77 (3) (1955) 793–798.
[49] H. Tamura, K. Goto, M. Nagayama, Effect of anions on oxygenation of ferrous ion in neutral solutions, J. Inorg. Nucl. Chem. 38 (1) (1976) 113–117.
[50] B. van der Grift, T. Behrends, L.A. Oste, P.P. Schot, M.J. Wassen, J. Griffioen, Fe hydrogenphosphate precipitation and Fe(II) oxidation kinetics upon aeration of Fe (II) and phosphate-containing synthetic and natural solutions, Geochem. Cosmochim. Acta 186 (2016) 71–90.
[51] M. Mallet, K. Barthelemy, C. Ruby, A. Renard, S. Naille, Investigation of phosphate adsorption onto ferrihydrite by X-ray Photoelectron Spectroscopy, J. Colloid Interface Sci. 407 (2013) 95–101.
[52] A.C. Senn, R. Kaegi, S.J. Hug, J.G. Hering, S. Mangold, A. Voegelin, Composition and structure of Fe(III)-precipitates formed by Fe(II) oxidation in water at near-neutral pH: interdependent effects of phosphate, silicate and Ca, Geochem. Cosmochim. Acta 162 (2015) 220–246.
[53] V. Santoro, M. Martin, P. Persson, C. Lerda, D. Said-Pullicino, G. Magnacca, L. Celi, Inorganic and organic P retention by coprecipitation during ferrous iron oxidation, Geoderma 348 (2019) 168–180.
[54] P.J. Thibault, D.G. Rancourt, R.J. Evans, J.E. Dutrizac, Mineralogical confirmation of a near-P:Fe=1:2 limiting stoichiometric ratio in colloidal P-bearing ferrihydrite-like hydrous ferric oxide, Geochem. Cosmochim. Acta 73 (2) (2009) 364–376.